

Effective Modulation of CNS Inhibitory Microenvironment using Bioinspired Hybrid-Nanoscaffold-Based Therapeutic Interventions

Letao Yang, Brian M. Conley, Susana R. Cerqueira, Thanapat Pongkulapa, Shenqiang Wang, Jae K. Lee,* and Ki-Bum Lee*

Central nervous system (CNS) injuries are often debilitating, and most currently have no cure. This is due to the formation of a neuroinhibitory microenvironment at injury sites, which includes neuroinflammatory signaling and non-permissive extracellular matrix (ECM) components. To address this challenge, a viscous interfacial self-assembly approach, to generate a bioinspired hybrid 3D porous nanoscaffold platform for delivering anti-inflammatory molecules and establish a favorable 3D-ECM environment for the effective suppression of the neuroinhibitory microenvironment, is developed. By tailoring the structural and biochemical properties of the 3D porous nanoscaffold, enhanced axonal growth from the dual-targeting therapeutic strategy in a human induced pluripotent stem cell (hiPSC)-based *in vitro* model of neuroinflammation is demonstrated. Moreover, nanoscaffold-based approaches promote significant axonal growth and functional recovery *in vivo* in a spinal cord injury model through a unique mechanism of anti-inflammation-based fibrotic scar reduction. Given the critical role of neuroinflammation and ECM microenvironments in neuroinhibitory signaling, the developed nanobiomaterial-based therapeutic intervention may pave a new road for treating CNS injuries.

Neuroinflammation and inhibitory signaling are known to critically affect the progress of many neurological disorders at both acute and chronic phases.^[1] For example, the restoration of disrupted neural circuitry after central nervous system (CNS) injuries (e.g., stroke, traumatic brain injury, and spinal cord injury [SCI]) is hampered by inhibitory microenvironments (e.g., chondroitin sulfate proteoglycans deposited in the form of an astroglial and fibrotic scar) that are often initiated by

neuroinflammatory processes (e.g., neurotoxic cytokines and metalloproteinase secretion).^[2] To this end, considerable effort has been put forth to develop effective biomaterial-based therapeutic approaches for alleviating inflammatory pathways or suppressing scar formation through stimuli-responsive drug delivery, guided immunomodulation, and controlled regulation of neuronal behaviors (e.g., axonal growth and neurite outgrowth).^[3] For example, synthetic polymer nanofiber and biomaterial (e.g., fibrin)-based scaffolds have accelerated nerve regeneration in SCI animal models via sustainable delivery of neurotrophic factors and mimicking healthy neural extracellular matrix (ECM).^[4] And, polypeptide-based hydrogels promoted neurogenesis of transplanted stem cells and improved functional outcomes by providing a permissive ECM environment for axonal growth.^[5] More recently, nanomaterial (e.g., carbon nanotube and graphene)-

based hybrid bioscaffolds have shown multi-functionalities, including high-resolution *in vivo* imaging/stimulation and drug delivery, which has enabled the enhancement of their therapeutic effects after CNS injuries.^[6–8] Despite their huge potential, limited success in the clinical translation of nano/biomaterials has been achieved.^[3,9] This could be largely attributed to the dynamic and complex nature of the neuroinhibitory microenvironment.^[10] For instance, recent evidence strongly suggests that targeting neuroinflammation or inhibitory ECM components alone is insufficient to promote motor function recovery after CNS injuries, but few biomaterials have successfully targeted both inhibitory factors.^[11,12] Also, while a majority of biomaterial-based treatments of SCI have been focused on the reduction of the astroglial scar, researchers have recently drawn contradictory conclusions as to its therapeutic effect while also suggesting the fibrotic scar may play a critical role in the functional recovery of SCI animals.^[13] Taken together, it remains an ongoing challenge to design novel multifunctional biomaterials that address SCI therapeutic targets by effectively modulating the dynamic and complex neuroinhibitory microenvironment.

To address the aforementioned issues and facilitate the progress of *in vivo* drug/cell delivery, herein we developed a 3D-biodegradable porous hybrid (3D-BPH) nanoscaffold to synergistically

Dr. L. Yang, B. M. Conley, T. Pongkulapa, S. Wang, Prof. K.-B. Lee
Department of Chemistry and Chemical Biology
Rutgers
The State University of New Jersey
123 Bevier Road, Piscataway, NJ 08854, USA
E-mail: kblee@rutgers.edu

Dr. S. R. Cerqueira, Prof. J. K. Lee
Miami Project to Cure Paralysis
Department of Neurological Surgery
University of Miami School of Medicine
1095 NW 14th Terrace, LPLC 4–19, Miami, FL 33136, USA
E-mail: JLee22@med.miami.edu

 The ORCID identification number(s) for the author(s) of this article can be found under <https://doi.org/10.1002/adma.202002578>.

DOI: 10.1002/adma.202002578

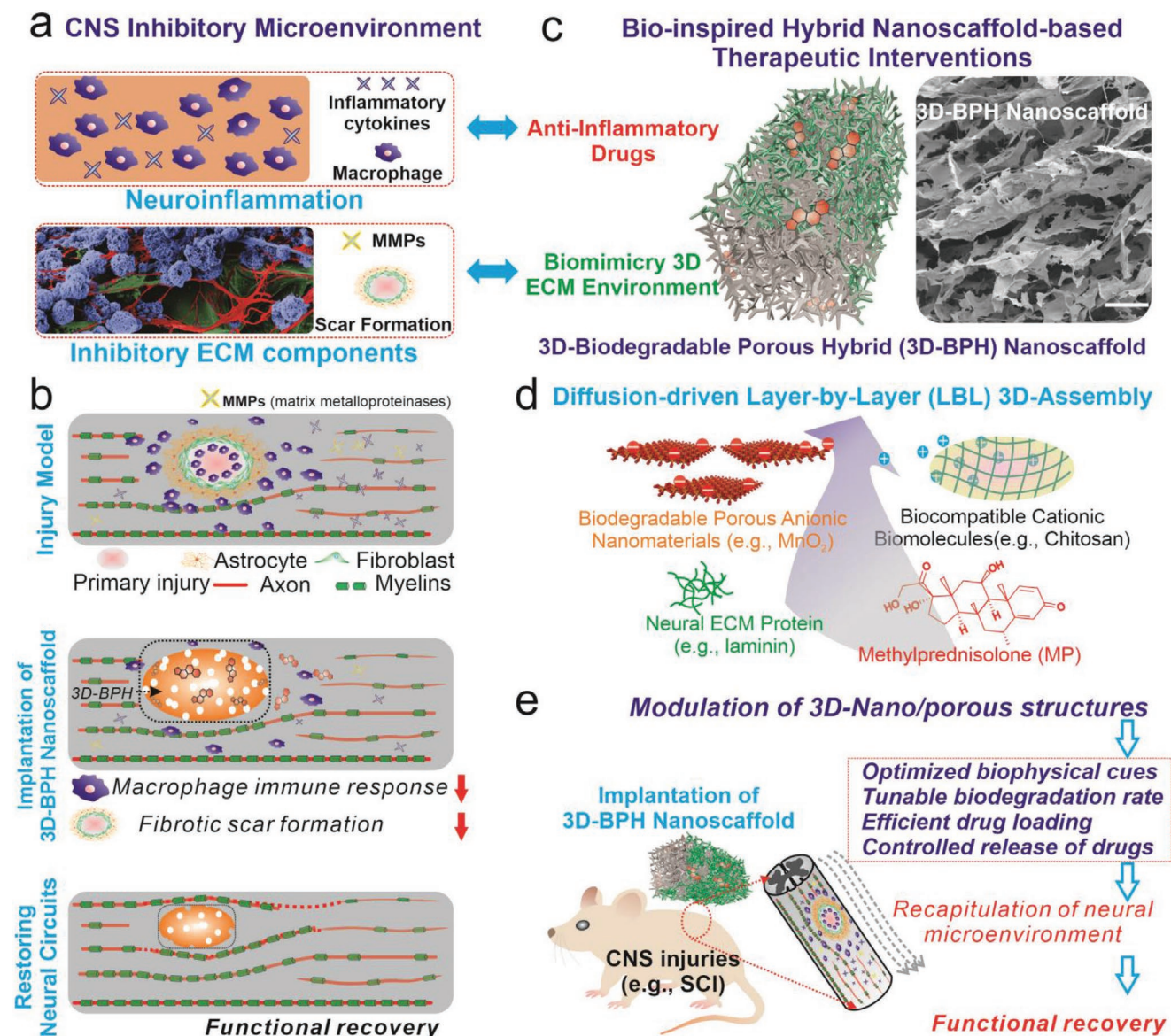


Figure 1. Effective modulation of inhibitory CNS microenvironment for the enhanced treatment of CNS injuries by developing bioinspired 3D-BPH nanoscaffold. a) A schematic illustration of the inhibitory microenvironment after CNS injury, which includes neuroinflammation and inhibitory ECM. In the “neuroinflammation” panel, blue-colored cells refer to macrophages and blue cross-refer to inhibitory cytokines. In the “inhibitory ECM components” panel, blue, red, and green refer to the cell body, neurites, and ECM of neurons, respectively. b) A proposed strategy for the effective modulation of CNS microenvironment after injuries by developing a 3D-BPH nanoscaffold-based therapeutic interventions. c) A schematic diagram (left) and field-emission scanning electron microscopy (FE-SEM, the image on the right) illustrating the structure and composition of 3D-BPH nanoscaffold designed for overcoming inhibitory microenvironments synergistically. Scale bar in FE-SEM: 100 μm . d) The 3D-BPH nanoscaffold is assembled from a unique viscous interfacial LBL 3D electrostatic assembly from anionic nanomaterials and cationic polymers, which simultaneously allows loading of an anti-inflammatory drug (methylprednisolone, MP, colored in red) and absorption of favorable neural ECM protein (e.g., laminin, colored in green). e) A schematic diagram illustrating the implantation of MP-loaded anti-inflammatory 3D-BPH nanoscaffold for the treatment of CNS injury by using a murine hemisection SCI model.

modulate the inhibitory microenvironment by combining the delivery of anti-inflammatory compounds (methylprednisolone (MP)) and reducing fibrotic scarring for the enhanced treatment of SCI (Figure 1a,b). This is achieved through designing a 3D-BPH nanoscaffold that demonstrates several unique structural, biological, and physicochemical properties by: i) creating a 3D-biomimetic matrix permissive to neural growth; ii) releasing therapeutic molecules (e.g., anti-neuroinflammatory drugs) in a

spatiotemporally controlled manner; iii) tuning the biodegradation rate of 3D-BPH nanoscaffold precisely; and iv) producing in vivo (magnetic resonance imaging [MRI]) neural imaging modalities in response to the scaffold-degradation process and drug release (Figure 1c). To achieve these ideal properties of nanobioscaffolds, our 3D-BPH nanoscaffold system was carefully designed and synthesized by employing a unique viscous interfacial layer-by-layer (LBL) 3D-electrostatic assembly of biocompatible

cationic polymers (e.g., chitosan) and biodegradable nanomaterials (e.g., 2D manganese dioxide [2D-MnO₂] nanosheets), which allows the formation of 3D-ordered, porous scaffold structures tailored for the treatment of CNS injuries (Figure 1d). More specifically, we achieved biomimetic Young's modulus, controllable drug release, and tunable biodegradation by modulating the porosity and composition of our 3D-BPH nanoscaffold. Strikingly, this unique 3D-BPH nanoscaffold facilitated the formation of 3D neuronal networks and synergistically promoted axonal growth in a human-induced pluripotent stem cell-derived neural stem cell (hiPSC-NSC)-based neuroinflammation model by providing dual-functions of anti-inflammation and 3D-biomimetic neural matrix formation. Moreover, the transplantation of our 3D-BPH nanoscaffold in vivo into a murine SCI model suppressed neuroinflammation and fibrotic scarring, while significantly improving functional recovery and enhancing axonal growth. Taken together, by developing our 3D-BPH nanoscaffold for modulating neuroinhibitory microenvironments, we may provide new insights into the biomaterial-based treatment of CNS injuries.

First, we established a viscous interfacial 3D LBL assembly for generating 3D biodegradable porous structures from atomic thin 2D nanomaterials with molding capability, injectability, and high biocompatibility. 2D nanomaterial (e.g., graphene)-based hybrid scaffolds developed by our group, as well as others, have shown excellent protein absorption with a high surface-area-to-volume ratio, drug loading, and bioimaging properties that offer clear advantages over conventional bioscaffolds.^[8,14] However, currently, there is a lack of reliable methods to produce the desired biomimetic ordered 3D porous structures from biodegradable 2D MnO₂ nanomaterials without compromising their chemical stability, biocompatibility, and bioactivity.^[8,9,15,16] Inspired by a conventional electrostatic LBL technique as well as recent advancement of diffusion-driven 3D assembly of graphene nanosheets, we developed a synthetic route to generate our 3D-BPH nanoscaffolds from a biodegradable 2D nanomaterial (i.e., MnO₂ nanosheets) and a US Food and Drug Administration (FDA)-approved cationic polymer (i.e., chitosan), as a means to provide a clinically-relevant nanomaterial-based bioscaffold (Figure 2a).^[17] More specifically, 2D-MnO₂ nanosheets were first generated through liquid exfoliation (Figure S1, Supporting Information). To initiate the 3D electrostatic LBL assembly, a highly viscous droplet of chitosan solution (molecular weight: 190 000–310 000 Da, +40 mV zeta potential) was placed and incubated in a nanosheet solution (3–50 mV) (Figure 2a,b; Figure S1, Supporting Information). The transparent droplet of chitosan then slowly expanded into a dark-colored gel-like macrostructure via step-by-step complexation between the negatively charged nanosheets and positively charged chitosan macromolecules (Figure 2b). After 2D-MnO₂ nanosheets and chitosan underwent 3D-LBL complexation, lyophilization then produced a mechanically robust, flexible, and airy 3D-scaffold, suggesting a highly porous nature of the hybrid scaffold (Figure 2b,c; Figure S2, Supporting Information). Interestingly, the free-standing structure preserved the 3D tubular shape of the reaction vessel, suggesting a molding ability of our assembly method for potential uses in personalized treatment of patients with SCI (Figures S2,S3, Supporting Information). Additionally, we examined the mechanism of LBL 3D electrostatic assembly, by testing a different 2D nanomaterial with a negative surface charge, graphene oxide (GO, –35 mV), and another

cationic polymer, polyethyleneimine (PEI, +15 mV). While scaffolds composed of graphene or PEI may also be useful for other applications, we found that structures assembled from GO do not degrade, and PEI induces unhealthy NSC morphology, a sign of poor biocompatibility, both of which are consistent with literature reports (Figure 2d; Figure S3, Supporting Information).^[8,18] Moreover, we found that 3D-BPH nanoscaffolds can be implanted through a clinically relevant syringe needle. Recently developed injectable scaffolds and hydrogels have advantages in terms of minimal invasiveness during surgery.^[19] Here, 3D-BPH nanoscaffold can be flowed through the syringe and injected into an artificial soft tissue (calcium-crosslinked alginate hydrogel) (Figure S4, Supporting Information). Overall, with these unique properties, our LBL 3D electrostatic assembly strategy could represent an advantageous method to produce 3D-porous nanoscaffolds for general tissue engineering applications.

Next, we sought to manipulate the porosity of 3D-BPH nanoscaffolds to achieve biomimetic mechanical properties, and to control their drug release profiles and biodegradation speeds, all of which are critical for modulating the dynamic and complex neuroinhibitory microenvironments (Figure 3a).^[3,20] Although the control over these critical biomaterial properties has been demonstrated in several polymer-based systems, it is still an ongoing challenge for inorganic–organic hybrid 3D nanoscaffolds.^[21] Based on the mechanism of viscous interfacial LBL assembly, the pore size in 3D-BPH nanoscaffolds can be reduced by gradually decreasing the hydration layer trapped between two layers of electrostatic assembly, which is realized by merely increasing concentrations of 2D-MnO₂ nanosheets stepwise. FE-SEM, mercury intrusion porosimetry, fluorescence microscopy, as well as liquid cell atomic force microscopy (AFM) techniques all confirmed the expected trend of pore size distributions (Figure 3b; Figures S2,S5, Supporting Information). Afterward, we further showcase the control over the physiochemical properties of 3D-BPH nanoscaffold. First, a proper porosity range (between 100 and 50 μm conditions) was identified to correlate with the stiffness of a spinal cord tissue (around 20 kPa within a 2–40 kPa range), which is desired to avoid a mechanical mismatch and potential exacerbated immune response (Figure 3c).^[22] In parallel, we found that a higher porosity leads to accelerated biodegradation, and results in a faster drug release from the nanoscaffold. More specifically, to match the time-frame of the inflammatory response post-SCI, we demonstrated the feasibility of 3D-BPH nanoscaffold to deliver anti-inflammatory drugs in the scenario of SCI within an acute therapeutic window (24–72 h) at pore sizes of 50 μm, which rapidly releases drugs in the first 3 days, followed by a more sustainable release, that matches the typical inflammatory timescale in SCI for in vivo applications (Figure 3d).^[23] Also, we adjusted biodegradation rates (1–2 weeks decomposition) of 3D-BPH nanoscaffolds for neural regeneration, since fast erosion of the scaffold may not allow sufficient time for axonal growth, while slow biodegradation can result in chronic immune reactions from the host spinal cord tissue (Figure 3e; Figure S4, Supporting Information).^[3] Our simulation indicated that fluid exchange within the microporous structures of 3D-BPH nanoscaffolds might contribute to the scaffold's overall exposure to extracellular reductants, thereby inducing biodegradation as well (Figure S4,

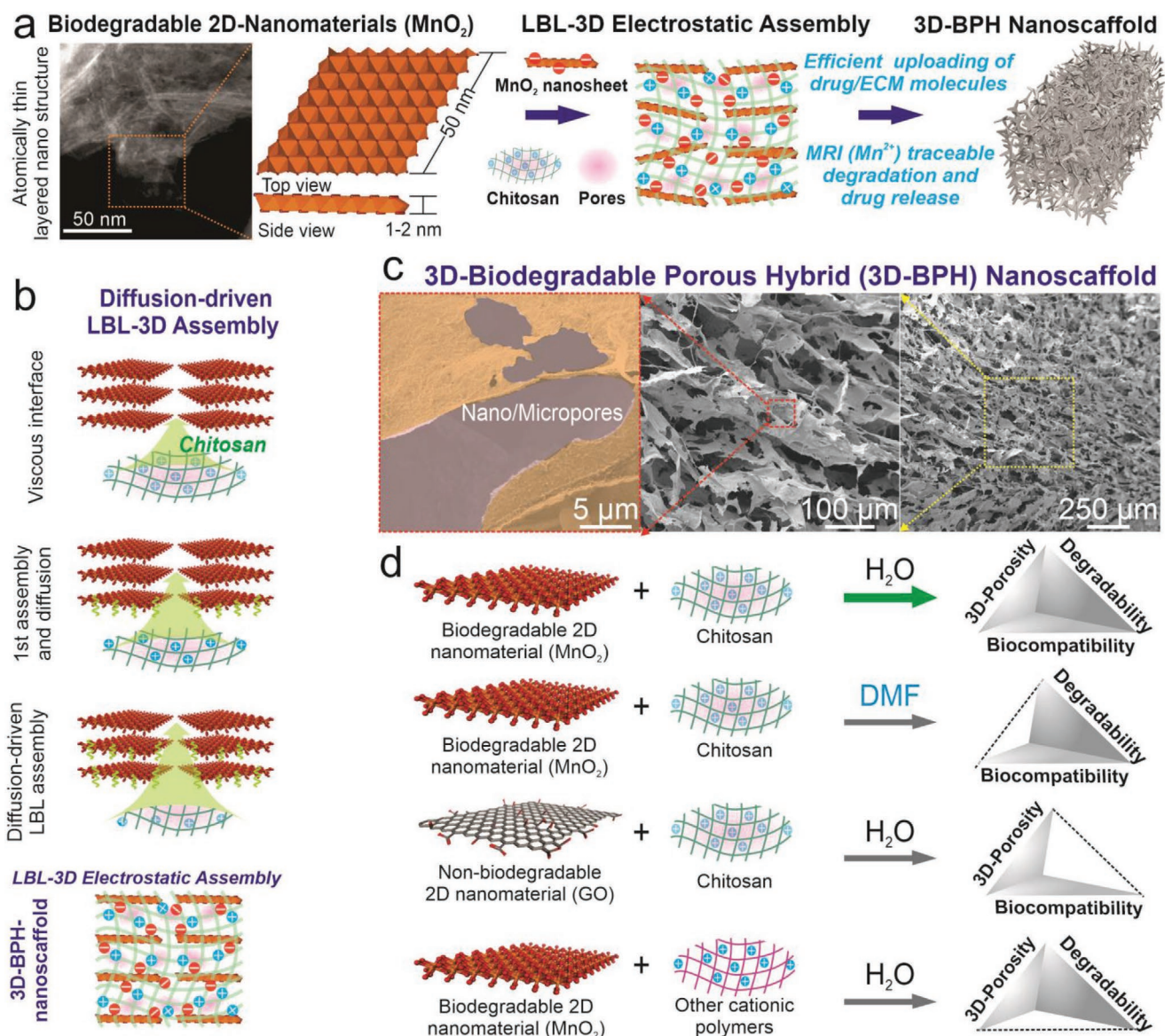


Figure 2. Multifunctional 3D-BPH nanoscaffold synthesized by viscous interfacial 3D electrostatic LBL self-assembly of biodegradable 2D nanomaterials and cationic polymers. a) A Schematic diagram showing the rationale for the synthesis of 3D-BPH nanoscaffold by assembling a biocompatible cationic polymer (chitosan) with biodegradable 2D nanosheets. b) A schematic diagram showing the detailed mechanism of viscous interfacial LBL 3D electrostatic assembly between negatively charged MnO_2 nanosheets and cationic polymer to form a 3D-hybrid hydrogel-like microstructure. By incubating a viscous droplet of chitosan solution in a nanosheet solution, the cationic polymer diffuses across the boundary between two solutions and binds to anionic nanosheets layer by layer until reach a balance. The scheme on the bottom shows the structure of the 3D-BPH nanoscaffold after lyophilization. The pink color represents micropores. c) FE-SEM images characterizing the generation of an ordered hierarchical porous network of 3D-BPH nanoscaffolds. d) Generalized synthesis of 3D-porous nanoscaffolds using differently charged macromolecules based on the LBL 3D electrostatic assembly as well as the solvent effects on the porosity formation. Among all the building blocks, the 3D-BPH nanoscaffold assembled from MnO_2 nanosheets, and chitosan with aqueous solvent has all desired properties for modulating neuroinhibitory microenvironments.

Supporting Information). Moreover, 3D-BPH nanoscaffold showed several distinctive properties compared to conventional polymeric scaffolds. First, the 3D-BPH nanoscaffold (average pore size of 50 μm) showed a high loading efficiency toward small molecule drugs with long-term maintenance of drug stability, likely mediated through metal- π and hydrophobic interactions (Figures S4,S6, Supporting Information).^[14] Second, we demonstrated higher ECM protein (i.e., laminin) and growth factor absorption onto 3D-BPH nanoscaffolds, which could be

also facilitated by their high specific surface areas and suggests the potential to improve biomimicry of favorable neural microenvironments (Figure 3f; Figure S7, Supporting Information).^[24] Most importantly, we were able to check drug release from 3D-BPH nanoscaffolds through the use of MRI (Figure 3g,h; Figure S4, Supporting Information). This process can be an attractive approach to non-invasively monitor both drug release and scaffold degradation in vivo for potential applications in personalized medicine. Taken together, we established

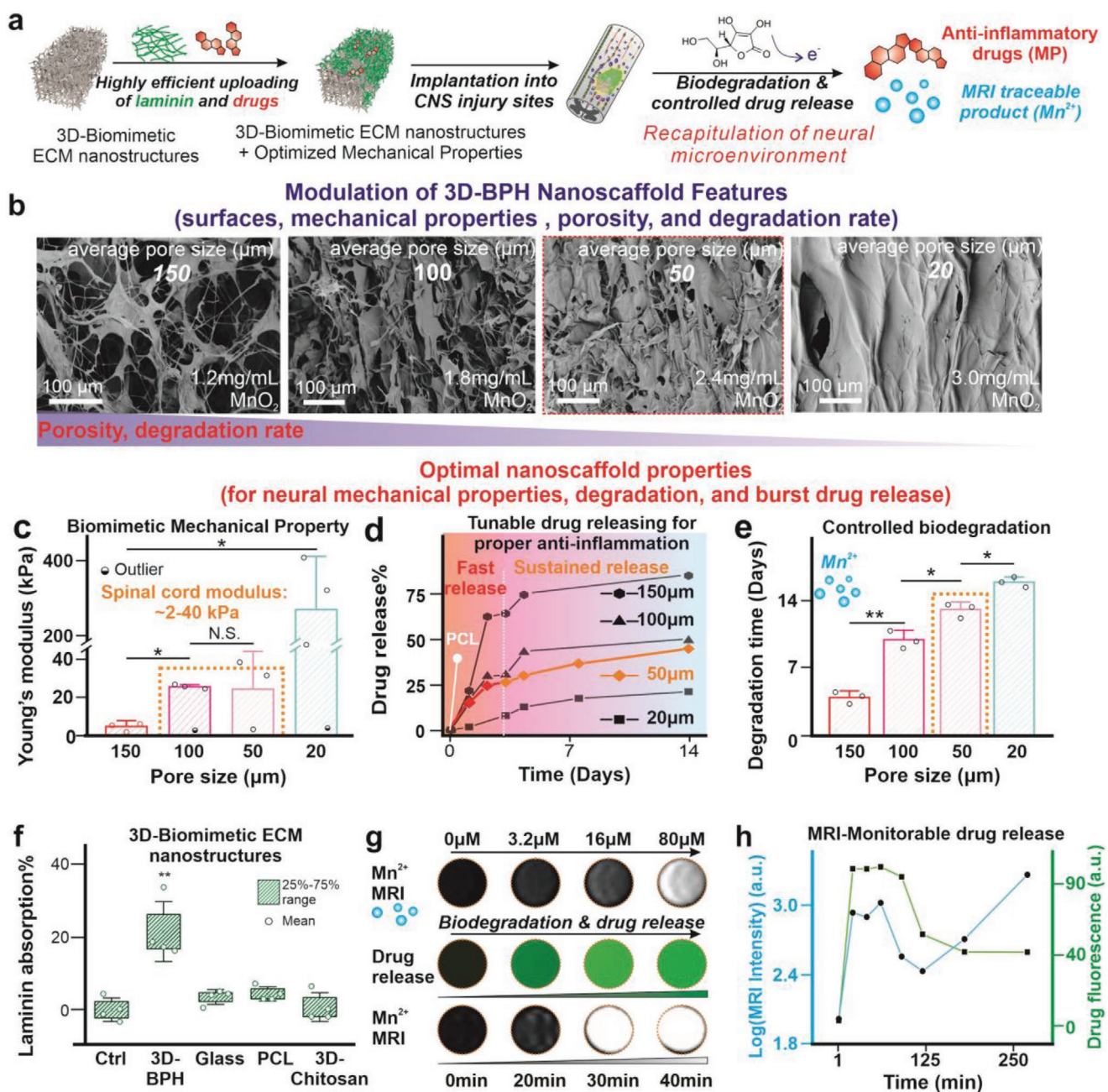


Figure 3. Achieving biomimetic mechanical property, and tailoring the degradation and drug release of 3D-BPH nanoscaffolds by tuning porous structures. a) A schematic diagram illustrating the development steps of the 3D-BPH nanoscaffold-based therapeutic platform and the critical scaffold considerations for our in vivo applications. b) FE-SEM images confirming the decrease of microporosities of 3D-BPH nanoscaffolds by manipulating the 3D-LBL self-assembly via increasing the concentrations of MnO_2 nanosheets. c) Modulation of Young's modulus of 3D-BPH nanoscaffolds with increasing MnO_2 nanosheet concentration characterized by AFM. The error bars are the standard deviation around the mean. $n = 3-4$ experimental replicates. Outliers are tested by Grubb's method. $*p < 0.05$, N.S. means no significance, by one-way analysis of variance (ANOVA) with Tukey post-hoc analysis. d) Tunable and sustainable drug delivery release profiles to match the resolution of inflammation post-SCI. The tunable release profiles were controlled by modulating the porosity of 3D-BPH nanoscaffolds. A control PCL nanoscaffold with burst release of drugs is shown in a white-colored line. e) The robust control of biodegradation speeds via tuning the porosity of 3D-BPH nanoscaffolds in the presence of an endogenous reductant at a concentration similar to the blood (ascorbic acid [$10 \mu\text{g mL}^{-1}$]). A higher porosity was found to lead to a faster degradation speed. The error bars are the standard deviation around the mean. $n = 3$ experimental replicates. $*p < 0.05$, $**p < 0.01$ by one-way ANOVA with Tukey post-hoc analysis. f) Bicinchoninic acid assay-based characterization of enhanced absorption toward laminin from 3D-BPH nanoscaffold compared to control scaffolds (glass and polymer [polycaprolactone and 3D-chitosan scaffolds]), which helps the creation of biomimicry ECM microenvironment. The box represents the 25–75% data range around the mean. $n = 4$ experimental replicates. $**p < 0.01$ by one-way ANOVA with Tukey post-hoc analysis. g) MRI monitoring of drug release from 3D-BPH nanoscaffold demonstrated by first establishing a standard Mn^{2+} concentration (top row), drug release (shown in green fluorescence in the middle row), and MRI signal of released Mn^{2+} (bottom row). h) Quantifications of the MRI-monitorable drug release in (g).

a reliable approach for uniquely modulating biochemical properties of inorganic–organic 3D hybrid scaffolds with a variety of advantages over conventional scaffold biomaterials.

The robust therapeutic effects of the developed 3D-BPH nanoscaffold for synergistically modulating the neuroinhibitory microenvironment were then demonstrated through an hiPSC-NSC-based neuroinflammation model (Figure 4a,b). The neuroinhibitory microenvironment is typically composed of both neuroinflammation and inhibitory ECM components, which have not been well addressed by previous biomaterial-based approaches.^[1,11] As such, we hypothesized that the 3D-BPH nanoscaffold could more effectively enhance neural regeneration, with its capabilities of tailoring drug-releasing profiles for anti-inflammation, and strongly adsorbing neural favorable ECM proteins. To demonstrate this, we first showcased the robust anti-inflammatory effects from the drug-loaded 3D-BPH nanoscaffold in a Transwell-based model by co-culture with human-monocyte-derived and lipopolysaccharide (LPS)-activated macrophages. For the selection of anti-inflammatory drugs, we loaded MP onto 3D-BPH nanoscaffold as a proof-of-concept, as it is currently the only clinically prescribed treatment for acute SCI (Figure S8, Supporting Information).^[25] We proved the robust anti-inflammatory effect from the MP-loaded 3D-BPH nanoscaffold, based on the substantially reduced expression of pro-inflammatory markers tumor necrosis factor (TNF), interleukin (IL), chemokine ligands (CCL) genes IL-4, and IL-13 (Figure S8, Supporting Information). In addition, as degradation of laminin by metalloproteinase (MMP) has been associated with inhibition of axonal growth after SCI, we also confirmed the reduced expression of MMP-1, MMP-2, and MMP-9 upon activation by LPS through the treatment of MP-loaded 3D-BPH nanoscaffold (MP-scaffold).^[25] This result could imply a unique synergy between anti-inflammation and the creation of a favorable ECM environment for promoting axonal growth by effectively downregulating the expression of pro-inflammatory cytokines and upregulating anti-inflammatory cytokines in activated macrophages.^[26] While direct treatment of macrophages by MP also showed anti-inflammatory effects, our nanoscaffold can offer spatially controlled release (Figure S6, Supporting Information) that can potentially reduce side effects from MP, such as global immune suppression, and can prolong therapeutic effects at SCI sites in vivo.^[27] Next, to demonstrate the synergistic effects between the creation of a permissive 3D ECM environment and reduction of neuroinflammation, we further performed an hiPSC-NSC-based in vitro assay on drug-loaded and laminin-functionalized 3D-BPH nanoscaffold. In this in vitro model, hiPSC-NSCs can provide an excellent platform that closely mimics the human CNS for disease modeling and immune modulation.^[28] We hypothesized that 3D-BPH nanoscaffold alone could enhance positive neuronal behaviors (e.g., axonal growth) by providing a biomimicry 3D ECM microenvironment, due to its significantly higher absorption toward laminin and the 3D biomimicry porous structures tailored for neural applications (Figure S9, Supporting Information). We confirmed our hypothesis by observing a nearly twofold increase of axonal lengths as well as the formation of 3D neuronal networks of hiPSC-NSC-differentiated neurons on the 3D-BPH nanoscaffold under normal culture conditions (without inflammation) (Figure S10, Supporting Information, Figure 4c,d,g).

Then, we verified that 3D-BPH nanoscaffold could be further combined with anti-inflammatory approaches for synergistically enhancing cell survival, neuronal differentiation, and axonal growth in our hiPSC-NSC-based neuroinflammation co-culture model (Figure 4e–j). As control groups, 3D-BPH nanoscaffold without the loaded drug (scaffold), laminin-coated chitosan, and laminin-coated glass substrates were seeded with hiPSC-NSCs cultured in the upper layer of the Transwell system. In this system, secreted pro-inflammatory cytokines and chemokines interacted with hiPSC-NSCs in the top chamber, mimicking a post-injury inflammatory microenvironment. After seven days in neuronal differentiation media, both laminin-coated chitosan and 3D-BPH nanoscaffolds showed similar enhancement of cell survival compared to the glass substrates (significant with $p < 0.05$) (Figure 4f,h), which is consistent with the laminin absorption assay (Figure 3f), as laminin is known to play a critical role in supporting the survival of neural stem cells.^[4] However, neuronal differentiation shows a similar trend in the healthy culture (non-inflammatory) condition, with enhancement only existent in the 3D-BPH nanoscaffolds but not in the laminin-coated chitosan scaffolds. Most importantly, the enhancement of axonal growth is only significant in MP-3D-BPH nanoscaffold condition, thereby proving the additional therapeutic effects from the sustainable delivery of the anti-inflammatory drug MP ($p < 0.001$, 0.01, and 0.05 compared to the laminin-coated glass, chitosan, and 3D-BPH nanoscaffolds, respectively) (Figure 4g,i,j).

Therefore, in the neuroinflammation model used by our nanoscaffold platform, a synergistic effect from anti-inflammation and creation of biomimetic 3D-ECM environment on promoting neuronal behaviors (e.g., neurogenesis and axonal growth) were strongly supported, suggesting a potential for in vivo applications.

With the encouraging results from the in vitro neuroinflammation assay, we went on to study the 3D-BPH nanoscaffold-facilitated enhanced axonal growth and functional recovery in a spinal cord injury model in vivo. Systemic delivery of MP is currently the only clinical standard for treating acute SCI, but it is no longer widely used due to complications resulting from global immunosuppression.^[25] Although several nanobiomaterial-based drug delivery approaches have been developed for reducing astroglial scarring and improving the treatment of CNS injuries, recent evidence suggests it is essential to overcome multiple therapeutic targets within the neuroinhibitory microenvironment, which includes the fibrotic scarring that is often overlooked in terms of their critical role in the functional recovery of SCI.^[11–13] To this end, we performed a Thoracic 8 (T8) spinal cord dorsal hemisection injury in mice and immediately implanted the MP-scaffold or the laminin-coated scaffold-only control (scaffold) in the lesion site to investigate the therapeutic effects of 3D-BPH nanoscaffold. We hypothesized that the MP-scaffold treatment would lead to improved pathology and functional recovery of SCI. First, we used a quantitative real-time polymerase chain reaction to investigate the effects of MP-scaffold on neuroinflammation in vivo and demonstrated the reduced expression of a subset of pro-inflammatory cytokine genes (TNF, IL1b, IL6, CCL2, and CCL5) (Figure 5c; Tables S1,S2, Supporting Information). The anti-inflammatory effects in the MP-scaffold group were also indicated by a

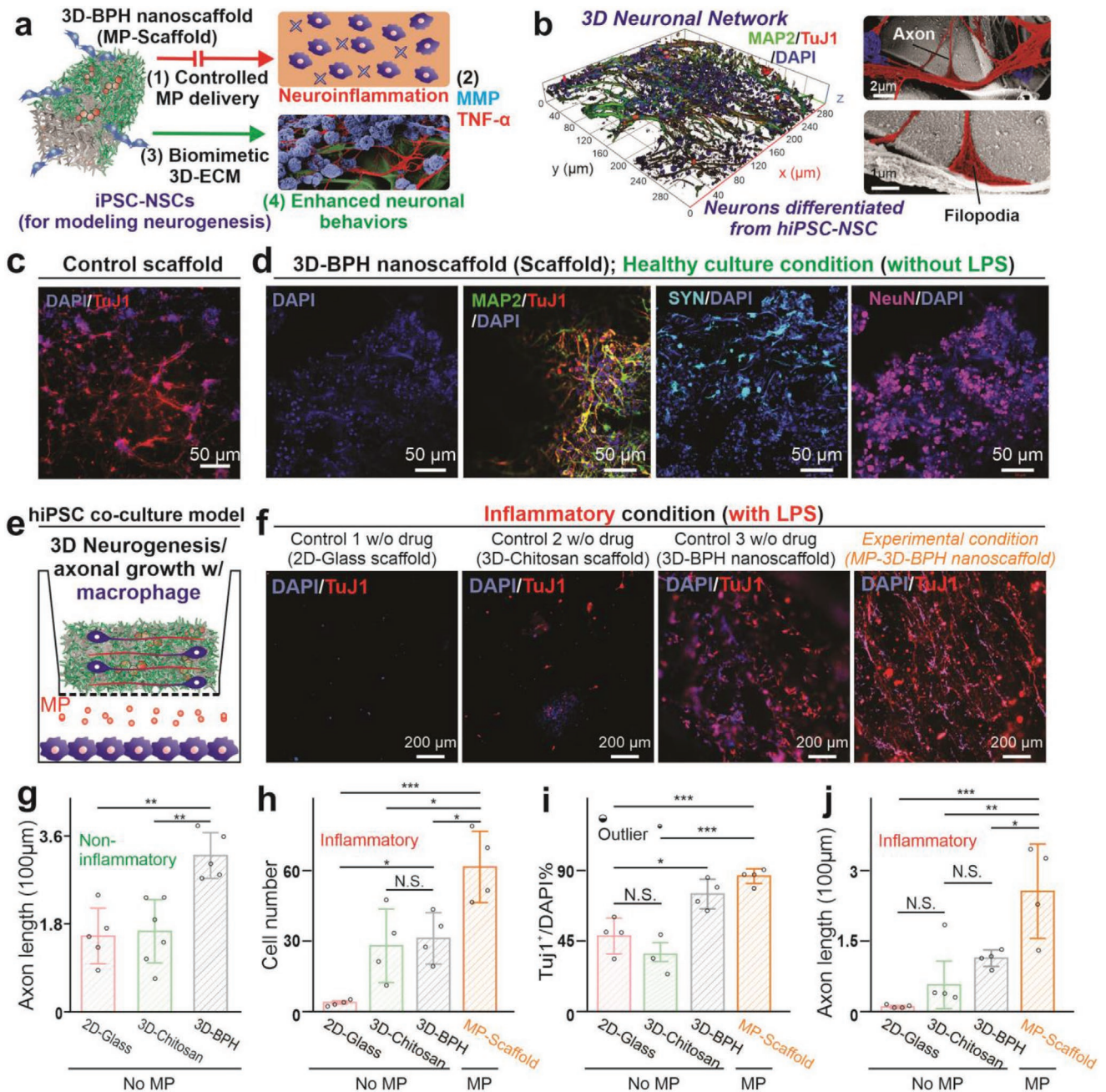


Figure 4. 3D-BPH nanoscaffolds promote 3D-neurogenesis and axonal growth under inflammatory microenvironments by providing a favorable 3D ECM environment and controlled anti-inflammatory drug delivery. a) A schematic diagram illustrating that macrophage-mediated inflammation produces neurotoxic cytokines (e.g., TNF) and ECM-degrading enzyme (e.g., MMP). The MP-loaded 3D-BPH nanoscaffold reduces this inhibitory signaling by reducing inflammation and providing a favorable 3D-ECM environment. b) A 3D-confocal image (on the left) and cell FE-SEM characterizations (on the right) showing the successful formation of the 3D neuronal network in the 3D-BPH nanoscaffold seeded with hiPSC-NSCs. c) A representative immunostaining image from hiPSC-NSCs differentiated on a control group (laminin-coated chitosan, 7 days after differentiation). d) Representative immunostaining images showing the expression of early (TuJ1, Day7) and mature (MAP2, SYN, NeuN, Day14) neuronal markers on the 3D neuronal network formed on 3D-BPH nanoscaffold under healthy culture (non-inflammatory) condition. e) A schematic diagram of neuroinflammation co-culture model. f) Representative immunostaining images confirming the improved neurogenesis and 3D-like neuronal network formation 7 days after differentiation from the anti-inflammatory MP-loaded 3D-BPH nanoscaffold (MP-3D-BPH) compared to the controls. g–j) Quantifications of the immunostaining results from control, 3D-BPH, and MP-3D-BPH nanoscaffolds under normal (g) or inflammatory conditions in terms of survival (h), neurogenesis (i), and axon growth (g,j). The error bars are the standard deviation around the mean, $n = 3–5$ experimental replicates. $*p < 0.05$, $**p < 0.01$, and $***p < 0.001$ by one-way ANOVA with Tukey post-hoc analysis. N.S. means no significance.

significant reduction in the density of infiltrating macrophages, as measured by the area of the cluster of differentiation molecule 11b (CD11b+) immunoreactivity (Figure 5d,g). Our findings

are well supported by literature and demonstrate the therapeutic effect of local scaffold-mediated MP release without global immune suppression.^[29] Next, we investigated the effects

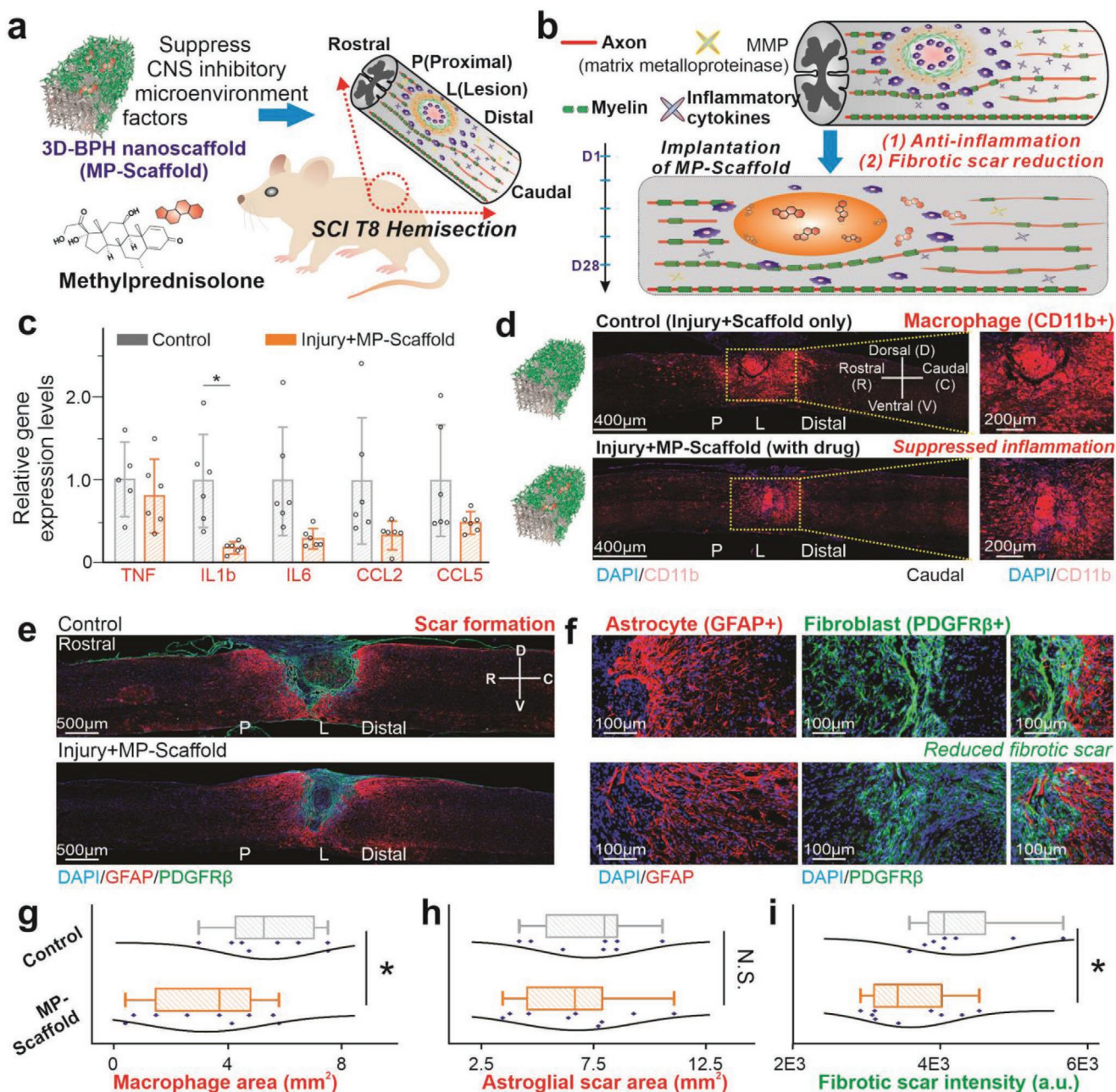


Figure 5. 3D-BPH nanoscaffold-mediated in vivo modulation of CNS inhibitory microenvironment post-SCI. a,b) Schematic diagrams illustrating the design of in vivo scaffold transplantation in a T8 dorsal hemisection mouse model to modulate the inhibitory microenvironment, which includes neuroinflammation and scar formation. c) Short-term (24 h) suppression of inflammatory genes in vivo by MP-scaffold compared to the control (injury followed by scaffold implantation only). The error bars are the standard deviation around the mean. $n = 5$ and 6 biological replicates for the control and experimental group, respectively. $*p < 0.05$ by Student's t -test. d) Long-term (28 days) suppression of inflammation in vivo by the MP-scaffold based on a macrophage marker, CD11b. e,f) Immunostaining images of tissue sections at the SCI sites characterizing the glial scar (GFAP, in red) and fibrotic (PDGFR β , in green) scar. g) Quantification of immune cell infiltration into the lesion based on the macrophage marker CD11b. $n = 8$ and 9 biological replicates for the control and experimental group, respectively. 4–5 sections of each animal were analyzed and averaged to obtain the individual data points. h,i) Quantification of the astroglial (h) and fibrotic (i) scar showing a decreased fibrotic scar formation in the MP-scaffold-treated conditions. The error bars are standard deviation around the mean. $*p < 0.05$ by Student's t -test. N.S. means no significance.

of MP-scaffold on fibrotic scarring post-SCI. Non-resolved SCI pathology is characterized by the formation and persistence of an astrocyte-rich border (astrocytic scar) surrounding the fibroblast dense lesion core (fibrotic scar).^[29,30] Recent reports have suggested that the reduction of the astroglial scar does

not aid the functional recovery of SCI animals.^[13,31] As such, we could effectively reduce the fibrotic scar and study its role in promoting functional recovery.^[30] We verified this based on a significant attenuation of the fibrotic scar, as measured by the intensity of platelet-derived growth factor subunit β

(PDGFR β^+), in the MP-scaffold group (Figure 5e–i; Figure S11, Supporting Information). Notably, MP-scaffold visibly reduced the dense fibrotic border adjacent to the astroglial scar. Meanwhile, evaluation of the glial scar formation revealed that the MP-scaffold implantation did not affect the reactivity of astrocytes and lesion size as measured by the glial fibrillary acidic protein (GFAP)-negative area compared to the scaffold-only group. Taken together, our results show that the local delivery

of MP through the 3D-BPH nanoscaffold reduces the inflammatory response, as well as the fibrotic scarring after SCI.

Moreover, we investigated the axonal growth and functional recovery from the suppressed neuroinflammation and selective reduction of fibrotic scarring (Figure 6a,b). Fibroblasts that accumulate in the lesion core after SCI are non-permissive for axonal growth, and reducing fibrotic scarring leads to increased axonal growth.^[31] We hypothesized that by reducing the fibrotic

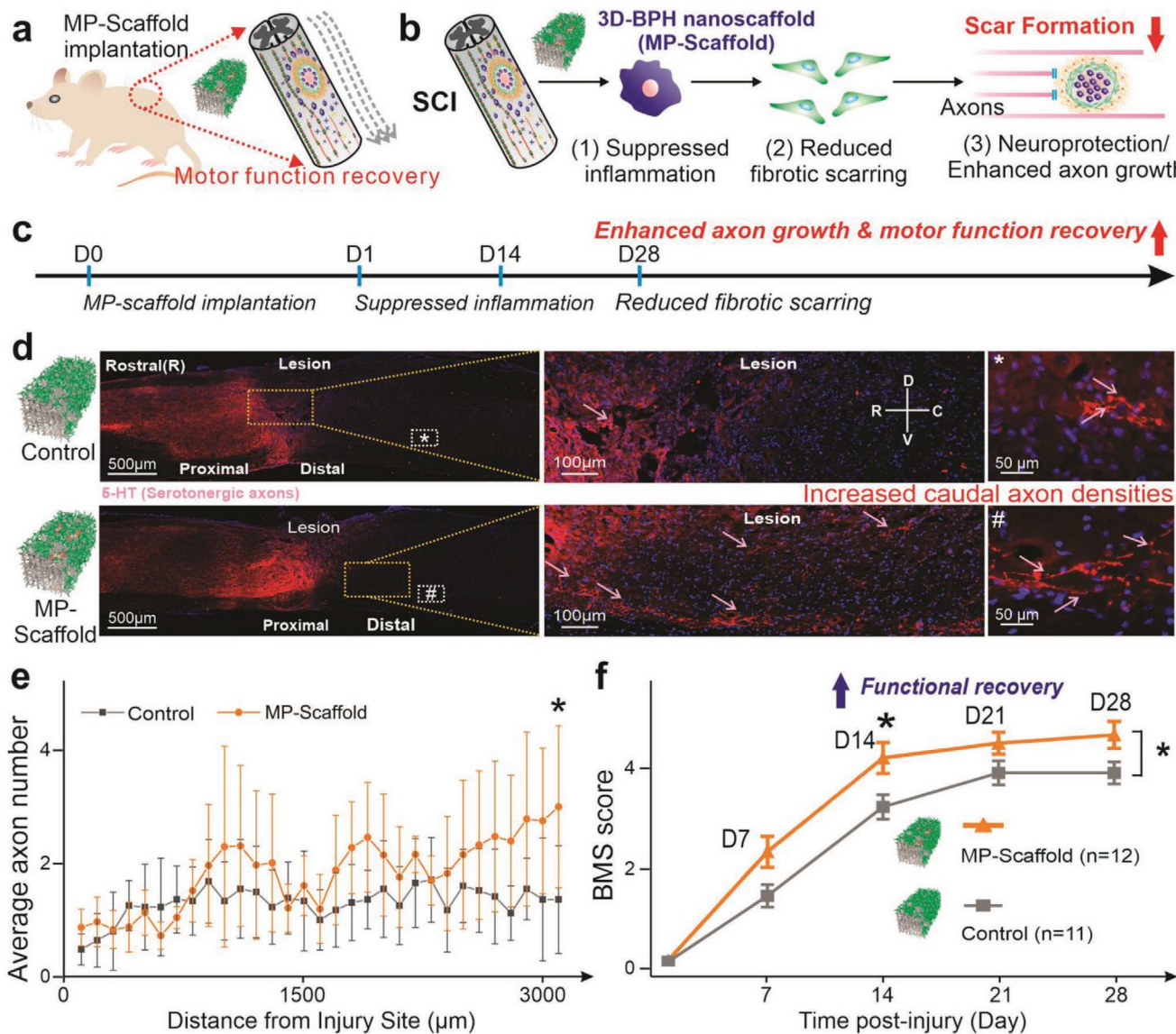


Figure 6. Reduced inhibitory microenvironment leads to enhanced caudal axonal densities and promotes functional recovery after SCI. a) A schematic diagram illustrating the transplantation of MP-scaffold in a mouse T8 hemisection model. b) Proposed mechanism for MP-scaffold-enhanced functional recovery by suppressed inflammation, reduced fibrotic scarring, and enhanced axonal growth. c) Timeline of the long-term in vivo experiments. d) Representative immunostaining images of the spinal cord from the control (SCI with scaffold implantation) and experimental (SCI with MP-scaffold implantation) conditions illustrating the overall serotonergic (5-HT) axonal density 28 days after the injury (left panel). Magnified views of the immunohistochemical staining images are shown in the middle and right panels, demonstrating the presence of axonal growth caudal to the lesion site (arrows indicate 5-HT labeled axons). e) Quantification of the distance-dependent distribution of axonal numbers (per section) 1-month post-injury show higher axonal density in the MP-scaffold-treated animal groups. Error bar represents standard deviation around the mean. * $p < 0.05$ by Student's t -test, $n = 7$ animals for both groups. 4–5 tissue sections were analyzed and then averaged for each animal. f) BMS scores of the control and experimental conditions indicating an accelerated functional recovery from the experimental condition compared to the control. Whereas most animals in the control group only achieved scores at dorsal stepping, the experimental group present significantly higher functional scores. $n = 12$ and 11 animals for the experimental group and control group, respectively. The error bars represent standard error around the mean. * $p < 0.05$ by Student's t -test in (e) and two-way ANOVA with Bonferonni post-test in (f).

scarring, axonal growth could be promoted effectively. This was confirmed by quantifying the number of serotonergic axons in the caudal region based on 5-HT immunostaining (Figure 6c,d; Figures S12,S13, Supporting Information). Among various subtypes of neurons in the spinal cord, 5-HT axons are descending fibers that have been reported to play essential roles in locomotor recovery after SCI.^[32] More specifically, while in both groups, we observed 5-HT axons caudal to the lesion site, a significantly higher number of 5-HT axons were found in the MP-scaffold group, suggesting a combined neuroprotective and regenerative effect from the MP-scaffold (Figure 6e). To study whether the enhanced axonal growth further improved locomotor behavioral recovery, Basso mouse scale (BMS) scoring was performed blindly on animals from the control and MP-scaffold group.^[33] Strikingly, we found that the MP-scaffold experimental group showed significantly better hindlimb locomotion than the scaffold-only group throughout the 1-month duration of this study. More specifically, MP-scaffold implantation produced significantly improved functional outcomes from as early as 14 days after SCI (Figure 6f). Taken together, our data demonstrate that local MP delivery to the injured spinal cord using 3D-BPH nanoscaffolds significantly decreased inflammatory cytokine expression, macrophage infiltration, and fibrotic scarring; thereby leading to improved functional outcomes after SCI. Both neuroinflammation and scar formation have been considered as critical factors for impeding functional recovery after CNS injuries.^[1] As such, our 3D-BPH nanoscaffold has excellent potential to treat CNS injuries by effectively tuning drug delivery rates and enhancing drug stability, while minimizing the side effects from systemic administration of drugs. Additionally, the enhanced functional recovery from the selective reduction of fibrotic scarring also indirectly supports recent findings undergoing the debate that reduced astroglial scarring does not aid the functional recovery of SCI.^[13] Taken together, the current work highlights the robust therapeutic potential of 3D-BPH nanoscaffolds to modulate the inhibitory SCI microenvironments and improve functional recovery, which is clinically relevant for developing novel treatments of SCI.

In summary, treating CNS injuries has been a significant challenge for decades due to the limited regenerative capacity of neurons and the neuroinhibitory microenvironment. To achieve an effective modulation of the multi-faceted neuroinhibitory microenvironment, we developed a 3D-BPH nanoscaffold through establishing a viscous interfacial 3D LBL self-assembly method. The 3D-BPH nanoscaffold achieved a biomimetic Young's modulus and showed tunable biochemical properties for anti-inflammatory applications as well as promoted neural cell behaviors through the formation of favorable neural ECM. We explored the synergistic effects of targeting both neuroinhibitory factors (neuroinflammation and inhibitory ECM) on the promotion of neural regeneration in vitro and demonstrated the enhanced treatment of SCI in vivo. It was found that a robust suppression of inflammation and a selective reduction of fibrotic scarring, promoted by a drug-loaded 3D-BPH nanoscaffold, directly improved axonal growth and functional recovery in vivo, implying an active role of scaffold-mediated suppression of the inhibitory microenvironment and functional recovery after CNS injuries. Moving forward, a comprehensive study on the mechanistic pathways in vivo would be essential

to confirm and understand the synergistic effect to improve the design of biomaterials in the treatment of SCI. The correlation of scaffold degradation to the release of MRI signals as well as the regeneration of the spinal cord in vivo could also encourage us to establish our 3D-BPH nanoscaffold as a precise therapeutic platform for personalized treatment of SCI. Furthermore, a comprehensive study on the systemic cytotoxic effects of the 3D-BPH nanoscaffold in a more relevant large animal model would be essential for the clinical translation of our therapeutic platform. Broadly, considering that neuroinflammation and deposition of inhibitory ECM components commonly exist in many different CNS injuries, a thorough investigation on the therapeutic effects of multifunctional biomaterials in different CNS injury models could provide novel perspectives on understanding the crosstalk among inflammation, ECM, and biomaterials that are crucial to treating CNS injuries.

Supporting Information

Supporting Information is available from the Wiley Online Library or from the author.

Acknowledgements

L.Y., B.C., and S.R.C. contributed equally to this work. K.-B.L. acknowledges the partial financial support from the NSF (CBET-1803517), the New Jersey Commission on Spinal Cord Research (CSCR17IRG010; CSCR16ERG019), NIH R21 (R21AR071101), and NIH R01 (1R01DC016612, 3R01DC016612-01S1, and 5R01DC016612-02S1). This work was also supported by NINDS R01NS081040 awarded to J.K.L., and NIH grant S10OD023579 for the VS120 Slide Scanner housed at the University of Miami Miller School of Medicine Analytical Imaging Core Facility. The authors acknowledge Shavin Patel, Yunlong Zhang, and Ha-Yeong Jeon, for assistance in the synthesis of nanoscaffolds. The authors are also grateful to Jeffery Luo, Dr. Hyeon-Yeol Cho, Dr. Jinho Yoon, and Christopher Rathnam for their help in the characterization of the scaffold. All animal procedures (Animal Welfare Assurance Number A3224-01, protocol no. 17-121; PI Jae K. Lee) were approved by the Institutional Animal Care and Use Committee of the University of Miami. Human iPSC-NSCs were provided by Dr. Muotri, UC San Diego. THP-1 monocyte cells were purchased from ATCC (catalog number: TIB-202).

Conflict of Interest

The authors declare no conflict of interest.

Keywords

biomaterials, inorganic–organic hybrid nanomaterials, nanoscaffolds, neural tissue engineering, spinal cord injury

Received: April 15, 2020

Revised: July 4, 2020

Published online:

[1] a) J. W. Fawcett, *Neurochem. Res.* **2020**, *45*, 144; b) X. Zhou, S. Wahane, M. S. Friedl, M. Kluge, C. C. Friedel, K. Avrampou,

- V. Zachariou, L. Guo, B. Zhang, X. J. He, R. H. Friedel, H. Y. Zou, *Nat. Neurosci.* **2020**, *23*, 337; c) J. G. Walsh, D. A. Muruve, C. Power, *Nat. Rev. Neurosci.* **2014**, *15*, 84.
- [2] a) D. W. Simon, M. J. McGeachy, H. Bayir, R. S. B. Clark, D. J. Loane, P. M. Kochanek, *Nat. Rev. Neurol.* **2017**, *13*, 171; b) G. Yiu, Z. G. He, *Nat. Rev. Neurosci.* **2006**, *7*, 617; c) L. M. Milich, C. B. Ryan, J. K. Lee, *Acta Neuropathol.* **2019**, *137*, 785.
- [3] a) W. Ong, C. Pinese, S. Y. Chew, *Adv. Drug Delivery Rev.* **2019**, *149–150*, 19; b) L. A. Rocha, D. Silva, S. Barata-Antunes, H. Cavaleiro, E. D. Gomes, N. A. Silva, A. J. Salgado, *Adv. Funct. Mater.* **2020**, *26*, 1909083.
- [4] I. E. Donaghue, R. Tam, M. V. Sefton, M. S. Shoichet, *J. Controlled Release* **2014**, *190*, 219.
- [5] a) A. E. Rochford, A. Carnicer-Lombarte, V. F. Curio, G. G. Williams, D. G. Barone, *Adv. Mater.* **2020**, *17*, 1903182; b) S. R. Li, L. R. Nih, H. Bachman, P. Fei, Y. L. Li, E. Nam, R. Dimatteo, S. T. Carmichael, T. H. Barker, T. Segura, *Nat. Mater.* **2017**, *16*, 953; c) P. Lu, Y. Wang, L. Graham, K. McHale, M. Gao, D. Wu, J. Brock, A. Blesch, E. S. Rosenzweig, L. A. Havton, *Cell* **2012**, *150*, 1264.
- [6] G. A. Silva, C. Czeisler, K. L. Niece, E. Beniash, D. A. Harrington, J. A. Kessler, S. I. Stupp, *Science* **2004**, *303*, 1352.
- [7] a) M. Srikanth, J. A. Kessler, *Nat. Rev. Neurol.* **2012**, *8*, 307; b) H. A. Ledesma, X. J. Li, J. L. Carvalho-de-Souza, W. Wei, F. Bezanilla, B. Z. Tian, *Nat. Nanotechnol.* **2019**, *14*, 645; c) B. Z. Tian, J. Liu, T. Dvir, L. H. Jin, J. H. Tsui, Q. Qing, Z. G. Suo, R. Langer, D. S. Kohane, C. M. Lieber, *Nat. Mater.* **2012**, *11*, 986; d) B. B. Zhang, W. Yan, Y. J. Zhu, W. T. Yang, W. J. Le, B. D. Chen, R. R. Zhu, L. M. Cheng, *Adv. Mater.* **2018**, *30*, 23.
- [8] L. T. Yang, S. T. D. Chueng, Y. Li, M. Patel, C. Rathnam, G. Dey, L. Wang, L. Cai, K. B. Lee, *Nat. Commun.* **2018**, *9*, 1.
- [9] L. L. Gong, L. N. Cao, Z. M. Shen, L. Shao, S. R. Gao, C. Zhang, J. F. Lu, W. D. Li, *Adv. Mater.* **2018**, *30*, 1705684.
- [10] a) A. P. Tran, J. Silver, *Science* **2015**, *348*, 285; b) J. Kipnis, *Science* **2016**, *353*, 766.
- [11] M. A. Anderson, T. M. O'Shea, J. E. Burda, Y. Ao, S. L. Barlaty, A. M. Bernstein, J. H. Kim, N. D. James, A. Rogers, B. Kato, A. L. Wollenberg, R. Kawaguchi, G. Coppola, C. Wang, T. J. Deming, Z. G. He, G. Courtine, M. V. Sofroniew, *Nature* **2018**, *561*, 396.
- [12] a) B. Ji, M. Li, S. Budel, R. B. Pepinsky, L. Walus, T. M. Engber, S. M. Strittmatter, J. K. Relton, *Eur. J. Neurosci.* **2005**, *22*, 587; b) L. Olson, *Exp. Neurol.* **2013**, *248*, 309.
- [13] M. A. Anderson, J. E. Burda, Y. Ren, Y. Ao, T. M. O'Shea, R. Kawaguchi, G. Coppola, B. S. Khakh, T. J. Deming, M. V. Sofroniew, *Nature* **2016**, *532*, 195.
- [14] a) A. Solanki, S. T. D. Chueng, P. T. Yin, R. Kappera, M. Chhowalla, K. B. Lee, *Adv. Mater.* **2013**, *25*, 5477; b) S. Shah, P. T. Yin, T. M. Uehara, S. T. D. Chueng, L. Yang, K. B. Lee, *Adv. Mater.* **2014**, *26*, 3673; c) W. Tang, W. P. Fan, W. Z. Zhang, Z. Yang, L. Li, Z. T. Wang, Y. L. Chiang, Y. J. Liu, L. M. Deng, L. C. He, Z. Y. Shen, O. Jacobson, M. A. Aronova, A. Jin, J. Xie, X. Y. Chen, *Adv. Mater.* **2019**, *31*, 1900404; d) G. Dey, L. Yang, K.-B. Lee, L. Wang, *J. Phys. Chem. C* **2018**, *122*, 29017.
- [15] J. Koffler, W. Zhu, X. Qu, O. Platoshyn, J. N. Dulin, J. Brock, L. Graham, P. Lu, J. Sakamoto, M. Marsala, S. C. Chen, M. H. Tuszynski, *Nat. Med.* **2019**, *25*, 263.
- [16] Z. M. Liu, M. L. Tang, J. P. Zhao, R. J. Chai, J. H. Kang, *Adv. Mater.* **2018**, *30*, 20.
- [17] a) I. Ichinose, S. Mizuki, S. Ohno, H. Shiraishi, T. Kunitake, *Polym. J.* **1999**, *31*, 1065; b) J. Zou, F. Kim, *Nat. Commun.* **2014**, *5*, 5254.
- [18] M. R. Molla, P. A. Levkin, *Adv. Mater.* **2016**, *28*, 1159.
- [19] a) S. A. Bencherif, R. W. Sands, O. A. Ali, W. A. Li, S. A. Lewin, T. M. Braschler, T.-Y. Shih, C. S. Verbeke, D. Bhatta, G. Dranoff, D. J. Mooney, *Nat. Commun.* **2015**, *6*, 7556; b) J. Liu, T. M. Fu, Z. G. Cheng, G. S. Hong, T. Zhou, L. H. Jin, M. Duvvuri, Z. Jiang, P. Kruskal, C. Xie, Z. G. Suo, Y. Fang, C. M. Lieber, *Nat. Nanotechnol.* **2015**, *10*, 629.
- [20] a) S. Thuret, L. D. F. Moon, F. H. Gage, *Nat. Rev. Neurosci.* **2006**, *7*, 628; b) P. G. Popovich, E. E. Longbrake, *Nat. Rev. Neurosci.* **2008**, *9*, 481; c) S. David, A. Kroner, *Nat. Rev. Neurosci.* **2011**, *12*, 388.
- [21] S. J. Hollister, *Nat. Mater.* **2005**, *4*, 518.
- [22] a) E. S. Place, N. D. Evans, M. M. Stevens, *Nat. Mater.* **2009**, *8*, 457; b) A. Karimi, A. Shojaei, P. Tehrani, *J. Chem. Neuroanat.* **2017**, *86*, 15.
- [23] I. Pineau, S. Lacroix, *J. Comp. Neurol.* **2007**, *500*, 267.
- [24] a) M. Tang, Q. Song, N. Li, Z. Jiang, R. Huang, G. Cheng, *Biomaterials* **2013**, *34*, 6402; b) W. C. Lee, K. P. Loh, C. T. Lim, *Biomaterials* **2018**, *155*, 236; c) M. Chen, P. K. Patra, M. L. Lovett, D. L. Kaplan, S. Bhowmick, *J. Tissue Eng. Regen. Med.* **2009**, *3*, 269.
- [25] a) M. B. Bracken, M. J. Shepard, W. F. Collins, T. R. Holford, W. Young, D. S. Baskin, H. M. Eisenberg, E. Flamm, L. Leo-Summers, J. Maroon, *N. Eng. J. Med.* **1990**, *322*, 1405; b) M. Kiraz, E. Demir, *World Neurosurg.* **2020**, *136*, e504.
- [26] a) Z. Gu, J. Cui, S. Brown, R. Fridman, S. Mobashery, A. Y. Strongin, S. A. Lipton, *J. Neurosci.* **2005**, *25*, 6401; b) S. A. Busch, K. P. Horn, D. J. Silver, J. Silver, *J. Neurosci.* **2009**, *29*, 9967.
- [27] a) G. Orive, E. Anitua, J. L. Pedraz, D. F. Emerich, *Nat. Rev. Neurosci.* **2009**, *10*, 682; b) S. R. Cerqueira, J. M. Oliveira, N. A. Silva, H. Leite-Almeida, S. Ribeiro-Samy, A. Almeida, J. F. Mano, N. Sousa, A. J. Salgado, R. L. Reis, *Small* **2013**, *9*, 738; c) Y.-t. Kim, J.-M. Caldwell, R. V. Bellamkonda, *Biomaterials* **2009**, *30*, 2582.
- [28] R. G. Rowe, G. Q. Daley, *Nat. Rev. Genet.* **2019**, *20*, 377.
- [29] a) D. Bartholdi, M. E. Schwab, *Brain Res.* **1995**, *672*, 177; b) E. S. Fu, S. Saporta, *J. Neurosurg. Anesthesiol.* **2005**, *17*, 82; c) J. Park, Y. Zhang, E. Saito, S. J. Guczynski, B. B. Moore, B. J. Cummings, A. J. Anderson, L. D. Shea, *Proc. Natl. Acad. Sci. USA* **2019**, *116*, 14947.
- [30] a) F. Hellal, A. Hurtado, J. Ruschel, K. C. Flynn, C. J. Laskowski, M. Umlauf, L. C. Kapitein, D. Strikis, V. Lemmon, J. Bixby, *Science* **2011**, *331*, 928; b) C. F. Vogelaar, B. König, S. Krafft, V. Estrada, N. Brazda, B. Ziegler, A. Faissner, H. W. Müller, *PLoS One* **2015**, *10*, e0134371; c) E. J. Bradbury, E. R. Burnside, *Nat. Commun.* **2019**, *10*, 3879.
- [31] a) Y. Zhu, C. Soderblom, V. Krishnan, J. Ashbaugh, J. R. Bethea, J. K. Lee, *Neurobiol. Dis.* **2015**, *74*, 114; b) M. C. Shearer, J. W. Fawcett, *Cell Tissue Res.* **2001**, *305*, 267.
- [32] C. Soderblom, D. H. Lee, A. Dawood, M. Carballosa, A. J. Santamaria, F. D. Benavides, S. Jergova, R. M. Grumbles, C. K. Thomas, K. K. Park, J. D. Guest, V. P. Lemmon, J. K. Lee, P. Tsoufas, *eNeuro* **2015**, *2*, ENEURO.0001-15.2015.
- [33] D. M. Basso, L. C. Fisher, A. J. Anderson, L. B. Jakeman, D. M. McTigue, P. G. Popovich, *J. Neurotrauma* **2006**, *23*, 635.